

Numerical Methods for the Stochastic Landau-Lifshitz Navier-Stokes Equations

John B. Bell, Alejandro L. Garcia, Sarah A. Williams

Center for Computational Sciences and Engineering
Lawrence Berkeley National Laboratory
Berkeley, California, 94720, USA

Abstract

The Landau-Lifshitz Navier-Stokes (LLNS) equations incorporate thermal fluctuations into macroscopic hydrodynamics by using stochastic fluxes. This paper examines explicit Eulerian discretizations of the full LLNS equations. Several CFD approaches are considered (including MacCormack's two-step Lax-Wendroff scheme and the Piecewise Parabolic Method) and are found to give good results (about 10% error) for the variances of momentum and energy fluctuations. However, neither of these schemes accurately reproduces the density fluctuations. We introduce a conservative centered scheme with a third-order Runge-Kutta temporal integrator that does accurately produce density fluctuations. A variety of numerical tests, including the random walk of a standing shock wave, are considered and results from the stochastic LLNS PDE solver are compared with theory, when available, and with molecular simulations using a Direct Simulation Monte Carlo (DSMC) algorithm.

1 Introduction

Thermal fluctuations have long been a central topic of statistical mechanics, dating back to the light scattering predictions of Rayleigh (i.e., why the sky is blue) and the theory of Brownian motion of Einstein and Smoluchowski [1]. More recently, the study of fluctuations is an important topic in fluid mechanics due to the current interest in nanoscale flows, with applications ranging from micro-engineering [2, 3, 4] to molecular biology [5, 6, 7].

Microscopic fluctuations constantly drive a fluid from its mean state, making it possible to probe the transport properties by fluctuation-dissipation. This is the basis for light scattering in physical experiments and Green-Kubo analysis in molecular simulations. Fluctuations are dynamically important for fluids undergoing phase transitions, nucleation, hydrodynamic instabilities, combustive ignition, etc., since the nonlinearities can exponentially amplify the effect of the fluctuations.

In molecular biology, the importance of fluctuations can be appreciated by noting that a typical molecular motor protein consumes ATP at a power of roughly 10^{-16} watts while operating in a background of 10^{-8} watts of thermal noise power, which is likened to be “as difficult as walking in a hurricane is for us” [6]. While the randomizing property of fluctuations would seem to be unfavorable for the self-organization of living organisms, Nature has found a way to exploit these fluctuations at the molecular level. The second law of thermodynamics does not allow motor proteins to extract work from equilibrium fluctuations, yet the thermal noise actually assists the directed motion of the protein by providing the mechanism for overcoming potential barriers.

Following Nature’s example, there is interest in the fabrication of nano-scale devices powered by [8] or constructed using [9] so-called “Brownian motors.” Another application is in micro-total-analytical systems (μ TAS) or “lab-on-a-chip” systems that promise single-molecule detection and analysis [10]. Specifically, the Brownian ratchet mechanism has been demonstrated to be useful for biomolecular separation [11, 12] and simple mechanisms for creating heat engines driven by non-equilibrium fluctuations have been proposed [13, 14]. Finally, exothermic reactions, such as in combustion and explosive detonation, can depend strongly on the nature of thermal fluctuations [15, 16].

To incorporate thermal fluctuations into macroscopic hydrodynamics, Landau and Lifshitz introduced an extended form of the Navier-Stokes equations by adding stochastic flux terms [17]. The Landau-Lifshitz Navier-Stokes (LLNS) equations may be written as

$$\mathbf{U}_t + \nabla \cdot \mathbf{F} = \nabla \cdot \mathbf{D} + \nabla \cdot \mathbf{S} \tag{1}$$

where

$$\mathbf{U} = \begin{pmatrix} \rho \\ \mathbf{J} \\ E \end{pmatrix} \quad (2)$$

is the vector of conserved quantities (density of mass, momentum and energy). The hyperbolic flux is given by

$$\mathbf{F} = \begin{pmatrix} \rho \mathbf{v} \\ \rho \mathbf{v} \cdot \mathbf{v} + P \mathbf{I} \\ \mathbf{v} E + P \mathbf{v} \end{pmatrix} \quad (3)$$

and the diffusive flux is given by

$$\mathbf{D} = \begin{pmatrix} 0 \\ \tau \\ \tau \cdot \mathbf{v} + \kappa \nabla T \end{pmatrix}, \quad (4)$$

where \mathbf{v} is the fluid velocity, P is the pressure, T is the temperature, and $\tau = \eta(\nabla \mathbf{v} + \nabla \mathbf{v}^T - \frac{2}{3} \mathbf{I} \nabla \cdot \mathbf{v})$ is the stress tensor. Here η and κ are coefficients of viscosity and thermal conductivity, respectively, where we have assumed the bulk viscosity is zero.

The mass flux is microscopically exact but the other two flux components are not; for example, at molecular scales heat may spontaneously flow from cold to hot, in violation of the macroscopic Fourier law. To account for such spontaneous fluctuations, the LLNS equations include a stochastic flux

$$\mathbf{S} = \begin{pmatrix} 0 \\ \mathcal{S} \\ \mathcal{Q} + \mathbf{v} \cdot \mathcal{S} \end{pmatrix}, \quad (5)$$

where the stochastic stress tensor \mathcal{S} and heat flux \mathcal{Q} have zero mean and covariances given by

$$\langle \mathcal{S}_{ij}(\mathbf{r}, t) \mathcal{S}_{kl}(\mathbf{r}', t') \rangle = 2k_B \eta T (\delta_{ik}^K \delta_{jl}^K + \delta_{il}^K \delta_{jk}^K - \frac{2}{3} \delta_{ij}^K \delta_{kl}^K) \delta(\mathbf{r} - \mathbf{r}') \delta(t - t'), \quad (6)$$

$$\langle \mathcal{Q}_i(\mathbf{r}, t) \mathcal{Q}_j(\mathbf{r}', t') \rangle = 2k_B \kappa T^2 \delta_{ij}^K \delta(\mathbf{r} - \mathbf{r}') \delta(t - t'), \quad (7)$$

and

$$\langle \mathcal{S}_{ij}(\mathbf{r}, t) \mathcal{Q}_k(\mathbf{r}', t') \rangle = 0, \quad (8)$$

where k_B is Boltzmann's constant. The LLNS equations have been derived by a variety of approaches (see [17, 18, 19, 20]) and have even been extended to relativistic hydrodynamics [21]. While they were originally developed for equilibrium fluctuations (see Appendix A), specifically the Rayleigh and Brillouin spectral lines in light scattering, the validity of the LLNS equations for non-equilibrium systems has been derived [22] and verified in molecular simulations [23, 24].

In this paper we investigate a variety of numerical schemes for solving the LLNS equations. For simplicity, we restrict our attention to one-dimensional systems, so (1) simplifies to

$$\frac{\partial}{\partial t} \begin{pmatrix} \rho \\ J \\ E \end{pmatrix} = -\frac{\partial}{\partial x} \begin{pmatrix} \rho u \\ \rho u^2 + P \\ (E + P)u \end{pmatrix} + \frac{\partial}{\partial x} \begin{pmatrix} 0 \\ \frac{4}{3}\eta\partial_x u \\ \frac{4}{3}\eta u\partial_x u - \kappa\partial_x T \end{pmatrix} + \frac{\partial}{\partial x} \begin{pmatrix} 0 \\ s \\ q + us \end{pmatrix} \quad (9)$$

where

$$\begin{aligned} \langle s(x, t)s(x', t') \rangle &= \frac{1}{\sigma^2} \int dy \int dy' \int dz \int dz' \langle \mathcal{S}_{xx}(\mathbf{r}, t)\mathcal{S}_{xx}(\mathbf{r}', t') \rangle \\ &= \frac{8k_B\eta T}{3\sigma} \delta(x - x')\delta(t - t') \end{aligned} \quad (10)$$

and

$$\begin{aligned} \langle q(x, t)q(x', t') \rangle &= \frac{1}{\sigma^2} \int dy \int dy' \int dz \int dz' \langle \mathcal{Q}_x(\mathbf{r}, t)\mathcal{Q}_x(\mathbf{r}', t') \rangle \\ &= \frac{2k_B\kappa T^2}{\sigma} \delta(x - x')\delta(t - t') \end{aligned} \quad (11)$$

with σ being the surface area of the system in the yz -plane.

Furthermore, we take the fluid to be a dilute gas with equation of state $P = \rho RT$ and energy density $E = c_v\rho T + \frac{1}{2}\rho u^2$. The transport coefficients are only functions of temperature; for example, for a hard sphere gas $\eta = \eta_0\sqrt{T}$ and $\kappa = \kappa_0\sqrt{T}$, where η_0 and κ_0 are constants. The numerical schemes developed in this paper may readily be formulated for other fluids. Our choice is motivated by a desire to compare with molecular simulations (see Appendix B) of a monatomic, hard sphere gas (for which $R = k_B/m$ and $c_v = \frac{R}{\gamma-1}$ where m is the mass of a particle and the ratio of specific heats is $\gamma = \frac{5}{2}$).

Several numerical approaches for the Landau-Lifshitz Navier-Stokes (LLNS) equations, and related stochastic hydrodynamic equations, have been proposed. The most successful is a stochastic lattice-Boltzmann model developed by Ladd for simulating solid-fluid suspensions [25]. This approach for modeling the Brownian motion of particles was adopted by Sharma and Patankar [26] using a finite difference scheme that incorporates a stochastic momentum flux into the *incompressible* Navier-Stokes equations. By including the stochastic stress tensor of the LLNS equations into the lubrication equations Moseler and Landman [27] obtain good agreement with their molecular dynamics simulation in modeling the breakup of nanojets. An alternative mesoscopic approach to computational fluid dynamics, based on a stochastic description defined by a discrete master equation, is proposed by Breuer and Petruccione [28, 29]. They show that the structure of the resulting system recovers the fluctuations of LLNS.

Serrano and Español [30] describe a finite volume Lagrangian discretization of the continuum equations of hydrodynamics using Voronoi tessellation. Casting their model into the GENERIC structure [31] allows for the introduction of thermal fluctuations yielding a consistent discrete model for Lagrangian fluctuating hydrodynamics. Fabritiis et al. [32, 33] derive a similar mesoscopic, Voronoi-based algorithm using the dissipative particle dynamics (DPD) method. The dissipative particles follow the dynamics of extended objects subject to hydrodynamic forces, with stresses and heat fluxes given by the LLNS equations.

In earlier work Garcia, et al. [34] developed a simple finite difference scheme for the linearized LLNS equations. Though successful, that scheme was custom-designed to solve a specific problem; it cannot be extended readily, since it relies on special assumptions of zero net flow and constant heat flux and would be unstable in the more general case. Related finite difference schemes have been demonstrated for the diffusion equation [35], the “train” model [36], and the stochastic Burgers’ equation [37], specifically in the context of Adaptive Mesh and Algorithm Refinement hybrids that couple particle and continuum algorithms.

In the next section we develop three stochastic PDE schemes based on standard CFD schemes for compressible flow. The schemes are tested in a variety of scenarios in sections 3 and 4, measuring spatial and time correlations at equilibrium and away from equilibrium. Results are compared to theoretically derived values, and also to results from DSMC particle simulations (see Appendix B). We also examine the influence of fluctuations on shock drift, comparing results from the LLNS solver with DSMC simulations. The concluding section summarizes the results and discusses future work, with an emphasis on the issues related to using the resulting methodology as the foundation for a hybrid algorithm.

2 Numerical Methods

The goal here is to develop an Eulerian discretization of the full LLNS equations, representing an extension of the approach discussed in [37] to compressible flow. We restrict consideration here to finite-volume schemes in which all of the variables are collocated, so that the resulting method can form the basis of a hybrid method in which a particle description (DSMC) is coupled to the LLNS discretization. Within this class of discretizations, our aim is to recover the correct fluctuating statistics. In this section we develop two methods based on CFD schemes that are commonly used for the Navier-Stokes equations. We then introduce a specialized centered scheme designed to capture fluctuation intensities.

2.1 MacCormack Scheme

Based on the success of the simple second-order scheme in [34], we first consider MacCormack's variant of two-step Lax-Wendroff for solving fluctuating LLNS.¹ The MacCormack method is applied in the following way:

$$\begin{aligned}
\mathbf{U}_j^* &= \mathbf{U}_j^n - \frac{\Delta t}{\Delta x} (\mathbf{F}_j^n - \mathbf{F}_{j-1}^n) + \frac{\Delta t}{\Delta x} (\mathbf{D}_{j+1/2}^n - \mathbf{D}_{j-1/2}^n) \\
&\quad + \frac{\Delta t}{\Delta x} (\mathbf{S}_{j+1/2}^n - \mathbf{S}_{j-1/2}^n) \\
\mathbf{U}_j^{**} &= \mathbf{U}_j^* - \frac{\Delta t}{\Delta x} (\mathbf{F}_{j+1}^* - \mathbf{F}_j^*) + \frac{\Delta t}{\Delta x} (\mathbf{D}_{j+1/2}^* - \mathbf{D}_{j-1/2}^*) \\
&\quad + \frac{\Delta t}{\Delta x} (\mathbf{S}_{j+1/2}^* - \mathbf{S}_{j-1/2}^*) \\
\mathbf{U}_j^{n+1} &= \frac{1}{2} (\mathbf{U}_j^n + \mathbf{U}_j^{**}).
\end{aligned}$$

Here $\mathbf{D}_{j+1/2}^n$ is a simple finite difference approximation to \mathbf{D} .

Straightforward evaluation of \mathbf{S} would be

$$\mathbf{S}_{j+1/2} = \begin{pmatrix} 0 \\ s_{j+1/2} \\ q_{j+1/2} + u_{j+1/2} s_{j+1/2} \end{pmatrix}, \quad (12)$$

but we will see that some adjustment must be made. The approximation to the stochastic stress tensor, $s_{j+1/2}$, is computed as

$$s_{j+1/2}^n = \sqrt{\frac{4k_B}{3\Delta t V_c} (\eta_{j+1} T_{j+1} + \eta_j T_j)} \mathfrak{R}_{j+1/2}^n \quad (13)$$

where V_c is the volume of a cell and the \mathfrak{R} 's are independent, Gaussian distributed random values with zero mean and unit variance. The approximation to the discretized stochastic heat flux, $q_{j+1/2}$, is evaluated as

$$q_{j+1/2}^n = \sqrt{\frac{k_B}{\Delta t V_c} (\kappa_{j+1} (T_{j+1})^2 + \kappa_j (T_j)^2)} \mathfrak{R}_{j+1/2}^n. \quad (14)$$

These same stochastic flux approximations are used in all the continuum methods presented here.

The stochastic components of the flux, $\mathbf{S}_{j+1/2}^\ell$, are independent, identically distributed Gaussian random variables with mean zero and variance σ^2 for $\ell = n, *$. Substituting this into the MacCormack scheme we find that the variance in the flux at $j + 1/2$ is given by

¹A standard version of two-step Lax-Wendroff was also considered with similar but slightly poorer results.

$$\begin{aligned}
\left\langle \delta \left(\frac{1}{2} \mathbf{S}^n + \frac{1}{2} \mathbf{S}^* \right)^2 \right\rangle &= \left(\frac{1}{2} \right)^2 \langle \delta (\mathbf{S}^n)^2 \rangle + \left(\frac{1}{2} \right)^2 \langle \delta (\mathbf{S}^*)^2 \rangle \\
&= \left(\frac{1}{2} \right) \langle \delta (\mathbf{S}^n)^2 \rangle \\
&= \frac{\sigma^2}{2}.
\end{aligned}$$

That is, the variance in the flux is reduced to half its original magnitude by the averaging used in the two-step MacCormack algorithm. We correct this effect by replacing $\mathbf{S}_{j+1/2}$ with $\tilde{\mathbf{S}}_{j+1/2} = \sqrt{2}\mathbf{S}_{j+1/2}$. The MacCormack method we use is

$$\begin{aligned}
\mathbf{U}_j^* &= \mathbf{U}_j^n - \frac{\Delta t}{\Delta x} (\mathbf{F}_j^n - \mathbf{F}_{j-1}^n) + \frac{\Delta t}{\Delta x} (\mathbf{D}_{j+1/2}^n - \mathbf{D}_{j-1/2}^n) \\
&\quad + \frac{\Delta t}{\Delta x} (\tilde{\mathbf{S}}_{j+1/2}^n - \tilde{\mathbf{S}}_{j-1/2}^n) \\
\mathbf{U}_j^{**} &= \mathbf{U}_j^* - \frac{\Delta t}{\Delta x} (\mathbf{F}_{j+1}^* - \mathbf{F}_j^*) + \frac{\Delta t}{\Delta x} (\mathbf{D}_{j+1/2}^* - \mathbf{D}_{j-1/2}^*) \\
&\quad + \frac{\Delta t}{\Delta x} (\tilde{\mathbf{S}}_{j+1/2}^* - \tilde{\mathbf{S}}_{j-1/2}^*) \\
\mathbf{U}_j^{n+1} &= \frac{1}{2} (\mathbf{U}_j^n + \mathbf{U}_j^{**}).
\end{aligned}$$

2.2 Piecewise Parabolic Method

In [37] a piecewise linear second-order Godunov scheme was shown to be effective for solving the fluctuating Burgers' equation. We considered two versions of higher-order Godunov methods for the LLNS, a piecewise linear version [38] and the Piecewise Parabolic Method (PPM) introduced in [39]. The PPM algorithm, based on the direct Eulerian version presented in [40], produced considerably better results than the piecewise linear scheme. Since our goal is to preserve fluctuations, we do not limit slopes and we do not include discontinuity detection in the algorithm.

For this scheme the hyperbolic terms of the LLNS equations are considered in terms of hydrodynamic and local characteristic variables. In hydrodynamic variables we have

$$\frac{\partial}{\partial t} \mathbf{V} + \mathbf{A} \frac{\partial}{\partial x} \mathbf{V} = 0, \tag{15}$$

where

$$\mathbf{V}_j = \begin{pmatrix} \rho_j \\ u_j \\ P_j \end{pmatrix}. \tag{16}$$

The local characteristic variables are interpolated via a fourth-order scheme to the left (-) and right (+) edges of each cell:

$$\mathbf{W}_{j,\pm}^n = \frac{7}{12}(\mathbf{L}_j \mathbf{V}_j + \mathbf{L}_j \mathbf{V}_{j\pm 1}) - \frac{1}{12}(\mathbf{L}_j \mathbf{V}_{j\mp 1} + \mathbf{L}_j \mathbf{V}_{j\pm 2}), \quad (17)$$

where \mathbf{L}_j is the matrix whose rows are the left eigenvectors of \mathbf{A} evaluated at \mathbf{V}_j .

These values, together with the cell-centered value $\mathbf{W}_j^n = \mathbf{L}_j \mathbf{V}_j$, are used to construct a parabolic profile $\mathbf{W}_{j,k}(\theta)$ for each characteristic variable k in each cell,

$$\mathbf{W}(\theta) = \mathbf{W}_{j,-} + \theta \Delta \mathbf{W}_j + \theta(1 - \theta) \mathbf{W}_{j6}, \quad (18)$$

where

$$\begin{aligned} \theta &= \frac{x - (j - \frac{1}{2})\Delta x}{\Delta x}, \\ \Delta \mathbf{W}_j^n &= \mathbf{W}_{j,+}^n - \mathbf{W}_{j,-}^n, \text{ and} \\ \mathbf{W}_{j6}^n &= 6(\mathbf{W}_j^n - \frac{1}{2}(\mathbf{W}_{j,+}^n + \mathbf{W}_{j,-}^n)). \end{aligned}$$

Time-centered updates are based on the sign of each local characteristic wavespeed, $\lambda_{j,k}$:

$$\mathbf{W}_{j,\pm,k}^{n+1/2} = \begin{cases} \frac{1}{\nu_{j,k}} \int_{\pm\frac{1}{2} - \nu_{j,k}}^{\pm\frac{1}{2}} \mathbf{W}_{j,k}(\theta) d\theta, & \pm\lambda_{j,k} > 0 \\ \mathbf{W}_{j,\pm,k}^n & \text{otherwise} \end{cases}$$

where $\nu_{j,k} = \lambda_{j,k} \frac{\Delta t}{\Delta x}$.

Finally, the time-centered values are transformed back into primitive variables and used as inputs to a Riemann problem at each cell edge. We use the approximate Riemann solver discussed in [41]. This approach iterates the phase space solution in the $u - p$ plane, approximating the rarefaction curves by the Hugoniot locus. The overall approach is able to handle strong discontinuities and is second-order in wave strength.

Approximations to the viscous and stochastic flux terms are discussed in section 2.1. For our PPM algorithm we center the viscous update in time, so that the complete update is as follows:

$$\mathbf{U}_j^* = \mathbf{U}_j^n - \frac{\Delta t}{\Delta x} \mathbf{F}_j^n + \frac{\Delta t}{\Delta x} (\mathbf{D}_j^n + \tilde{\mathbf{S}}_j^n) \quad (19)$$

$$\mathbf{U}_j^{n+1} = \mathbf{U}_j^n - \frac{\Delta t}{\Delta x} \mathbf{F}_j^n + \frac{1}{2} \left(\frac{\Delta t}{\Delta x} \right) (\mathbf{D}_j^n + \tilde{\mathbf{S}}_j^n + \mathbf{D}_j^* + \tilde{\mathbf{S}}_j^*). \quad (20)$$

As discussed in section 2.1, for the PPM scheme we use the adjusted stochastic flux approximation $\tilde{\mathbf{S}}_j = \sqrt{2} \mathbf{S}_j$, since the averaging in the time-centering reduces the variance in the flux to half its original magnitude.

2.3 Variance-preserving third-order Runge-Kutta

Equilibrium tests, presented in detail in the next section, show that neither stochastic version of the traditional numerical methods discussed above accurately represents the fluctuations in the LLNS equations. The principal difficulty arises because there is no stochastic forcing term in the mass conservation equation. Accurately capturing density fluctuations requires that the fluctuations be preserved in computing the mass flux. Another key observation is that the representation of fluctuations in the above schemes is also sensitive to the time step, with extremely small time steps leading to somewhat improved results. This suggests that temporal accuracy also plays a significant role in capturing fluctuations. Based on these observations we have developed a new discretization aimed specifically at capturing fluctuations in the LLNS equations. The method is based on a third order Runge-Kutta temporal integrator (RK3) combined with a centered discretization of hyperbolic and diffusive fluxes.

The RK3 discretization can be written in the following three-stage form:

$$\mathbf{U}_j^{n+1/3} = \mathbf{U}_j^n - \frac{\Delta t}{\Delta x} (\mathcal{F}_{j+1/2}^n - \mathcal{F}_{j-1/2}^n) \quad (21)$$

$$\mathbf{U}_j^{n+2/3} = \frac{3}{4}\mathbf{U}_j^n + \frac{1}{4}\mathbf{U}_j^{n+1/3} - \frac{1}{4} \left(\frac{\Delta t}{\Delta x} \right) (\mathcal{F}_{j+1/2}^{n+1/3} - \mathcal{F}_{j-1/2}^{n+1/3}) \quad (22)$$

$$\mathbf{U}_j^{n+1} = \frac{1}{3}\mathbf{U}_j^n + \frac{2}{3}\mathbf{U}_j^{n+2/3} - \frac{2}{3} \left(\frac{\Delta t}{\Delta x} \right) (\mathcal{F}_{j+1/2}^{n+2/3} - \mathcal{F}_{j-1/2}^{n+2/3}), \quad (23)$$

where $\mathcal{F} = -\mathbf{F} + \mathbf{D} + \mathbf{S}$.

Combining the three stages, we can write

$$\mathbf{U}_j^{n+1} = \mathbf{U}_j^n - \frac{\Delta t}{\Delta x} \left[\frac{1}{6}(\mathcal{F}_{j+1/2}^n - \mathcal{F}_{j-1/2}^n) + \frac{1}{6}(\mathcal{F}_{j+1/2}^{n+1/3} - \mathcal{F}_{j-1/2}^{n+1/3}) + \frac{2}{3}(\mathcal{F}_{j+1/2}^{n+2/3} - \mathcal{F}_{j-1/2}^{n+2/3}) \right].$$

The stochastic components of the flux, $\mathbf{S}_{j+1/2}^{n+\ell}$ are independent, identically distributed Gaussian random variables with mean zero and variance σ^2 for $\ell = 0, \frac{1}{3}, \frac{2}{3}$. Substituting this into the combined update we find that the variance in the flux at $j + 1/2$ is given by

$$\begin{aligned} & \langle \delta \left(\frac{1}{6}(\mathbf{S}_{j+1/2}^0) + \frac{1}{6}(\mathbf{S}_{j+1/2}^{1/3}) + \frac{2}{3}(\mathbf{S}_{j+1/2}^{2/3}) \right)^2 \rangle \\ &= \left(\frac{1}{6} \right)^2 \langle (\delta \mathbf{S}_{j+1/2}^0)^2 \rangle + \left(\frac{1}{6} \right)^2 \langle (\delta \mathbf{S}_{j+1/2}^{1/3})^2 \rangle + \left(\frac{2}{3} \right)^2 \langle (\delta \mathbf{S}_{j+1/2}^{2/3})^2 \rangle \\ &= \frac{\sigma^2}{2}. \end{aligned}$$

Thus, in the course of the RK3 algorithm, the variance in the flux is reduced to half its original magnitude, so again we replace $\mathbf{S}_{j+1/2}$ by $\tilde{\mathbf{S}}_{j+1/2} = \sqrt{2}\mathbf{S}_{j+1/2}$, as discussed in section 2.1, and compute equations (21-23) using $\mathcal{F} = -\mathbf{F} + \mathbf{D} + \tilde{\mathbf{S}}$.

However, this treatment does not directly affect the fluctuations in density, since \mathbf{S} does not appear in the continuity equation. We can correct this effect via a special interpolation scheme: by augmenting the variance to compensate for the density reduction arising from the temporal averaging, the fluctuations are preserved in the mass flux computation.

We interpolate J (and the other conserved quantities) from cell-centered values:

$$J_{j+1/2} = \alpha_1(J_j + J_{j+1}) - \alpha_2(J_{j-1} + J_{j+2}), \quad (24)$$

where

$$\alpha_1 = (\sqrt{7} + 1)/4 \text{ and} \quad (25)$$

$$\alpha_2 = (\sqrt{7} - 1)/4. \quad (26)$$

Then in the case of constant J we have exactly $J_{j+1/2} = J$ and $\langle \delta J_{j+1/2}^2 \rangle = 2\langle \delta J^2 \rangle$, as desired; the interpolation is consistent and compensates for the variance-reducing effect of the multi-stage Runge-Kutta algorithm. The interpolation formula is similar to the PPM spatial construction except in the PPM construction $\alpha_1 = 7/12$ and $\alpha_2 = 1/12$. Tests based on these alternative weights produced results intermediate to the RK3 scheme and the PPM scheme. We also considered interpolation of primitive variables but found that interpolation based on primitive variables led to stable but undamped oscillatory behavior. Finally, the diffusive terms \mathbf{D} are discretized with standard second-order finite difference approximations.

2.4 Boundary Conditions

In sections 3 and 4 we consider test problems for the various PDE algorithms on either a periodic computational domain, a computational domain bounded by thermal walls, or a computational domain bounded by infinite reservoirs. Boundary conditions are implemented using ghost cells. For the periodic and reservoir boundaries, it is straightforward to determine the ghost cell data.

For the case of thermal walls, in addition to ghost cells we also use a one-sided finite difference formulation to approximate u_x and T_x in the calculation of the diffusive flux. The treatment of the hyperbolic flux at thermal walls varies by method.

For thermal wall boundaries in MacCormack, conserved quantities are reflected across the boundaries of the domain. The temperature in the ghost cells is determined by linear extrapolation, and the no-flow condition is enforced by setting the velocity terms of the hyperbolic flux to zero within the ghost cells.

For thermal wall boundaries in PPM, ghost cells are populated by reflecting primitive variable values across the domain boundaries, and the temperature in the ghost cells is determined by linear extrapolation. The PPM routine takes as input the cell-centered primitive

variable data and returns a Riemann solution at each cell edge. On the domain boundaries, we modify these Riemann solutions by enforcing fixed wall temperature (i.e., the pressure at the wall is taken to be a function of the fixed wall temperature) before computing the hyperbolic flux across each edge.

For thermal wall boundaries in RK3, conserved quantities are reflected across the boundaries of the domain and then interpolated onto cell edges. At the domain boundaries we employ a Riemann solver, which ensures that the boundary treatment respects characteristic compatibility relations at the physical boundaries. At the physical boundaries, the primitive variable values derived from the conserved-quantity interpolants are modified to enforce zero velocity and fixed wall temperature. This vector of primitive variables provides the input to the Riemann problem on the interior side of the boundary. The input to the Riemann problem on the exterior side of the boundary is the reflection of the interior input data. The treatment of reservoir boundaries is similar. However, ghost cells are populated with reservoir data, wall conditions are not enforced, and the input to the Riemann problem on the exterior side of the boundary is the reservoir data.

3 Numerical Tests – Equilibrium

This section presents results from a variety of scenarios in which the three schemes described above were tested. The physical domain is chosen to be compatible with DSMC particle simulations; see Table 1 for the system’s parameters and Appendix B for a description of DSMC. The domain is partitioned into 40 cells of equal size Δx and hyperbolic and diffusive stability constraints determine the maximum time step Δt :

$$(|u| + c_s) \frac{\Delta t}{\Delta x} \leq 1, \quad (27)$$

$$\max \left(\frac{4\bar{\eta}}{3\bar{\rho}}, \frac{\bar{\kappa}}{\bar{\rho}c_v} \right) \frac{\Delta t}{\Delta x^2} \leq \frac{1}{2}, \quad (28)$$

where the sound speed $c_s = \sqrt{\gamma\bar{P}/\bar{\rho}}$, $\bar{\eta} = \eta(\bar{T})$, and $\bar{\kappa} = \kappa(\bar{T})$; the overline indicates reference values (e.g., equilibrium values around which the system fluctuates). For the reference state (Argon at STP) and a cell width of $\Delta x \approx 10^{-6}$ cm the time step used was $\Delta t = 10^{-12}$ s.

3.1 Variances at equilibrium

The first benchmark for our numerical schemes is recovering the correct variance of fluctuations for a system at equilibrium. For this initial test problem, we take a periodic domain with zero net flow and constant average density and temperature. Similar results, not pre-

Molecular diameter (Argon)	3.66×10^8	Molecular mass (Argon)	6.63×10^{23}
Reference mass density	1.78×10^{-3}	Reference temperature	273
Sound speed	30781	Specific heat c_v	3.12×10^6
System length	1.25×10^{-4}	Reference mean free path	6.26×10^{-6}
System volume	1.96×10^{-16}	Time step	1.0×10^{-12}
Number of cells	40	Number of samples	10^7
Number of DSMC particles	5265	DSMC collision grid size	3.13×10^{-6}

Table 1: System parameters (in cgs units) for simulations of a dilute gas in a periodic domain.

sented here, were obtained for the case of constant non-zero net flow. The variances are computed in 40 spatial cells from 10^7 samples and then averaged over the cells.

Table 2 compares the theoretical variances (see Appendix A) with those measured in the three stochastic PDE schemes and the DSMC particle simulation. The MacCormack and PPM schemes do relatively poor job (9 – 16% error) for the variances of density and energy. Better PPM results are obtained by decreasing our value of Δt by a factor of 10, to 10^{-13} . However, it is not desirable to run simulations at such a small time step. Only the third-order Runge-Kutta integrator generates the correct variance of density and energy while advancing with time steps near the stability limit.

Table 2: Variance in conserved quantities at equilibrium (computed values are accurate to approximately 0.1%).

	$\langle \delta \rho^2 \rangle$	$\langle \delta J^2 \rangle$	$\langle \delta E^2 \rangle$
Exact value	2.35×10^{-8}	13.01	2.87×10^{10}
MacCormack scheme	2.01×10^{-8}	13.31	2.61×10^{10}
Piece-wise Parabolic Method	1.97×10^{-8}	13.27	2.58×10^{10}
Runge-Kutta (3 rd order)	2.32×10^{-8}	13.65	2.87×10^{10}
Molecular simulation (DSMC)	2.35×10^{-8}	13.21	2.79×10^{10}
Percentage difference (MacCormack)	−14.3%	2.3%	−9.3%
Percentage difference (PPM)	−16.0%	2.0%	−10.3%
Percentage difference (RK3)	−1.3%	4.9%	−0.1%
Percentage difference (DSMC)	0.0%	1.6%	−3.1%

3.2 Spatial correlations at equilibrium

Figures 1–3 depict the spatial correlation of conserved variables, that is, $\langle \delta\rho_j\delta\rho_{j^*} \rangle$, $\langle \delta J_j\delta J_{j^*} \rangle$, and $\langle \delta E_j\delta E_{j^*} \rangle$, where j^* is located at the center of the domain. These figures show results computed by the MacCormack, PPM, and RK3 schemes, along with the theoretical values of the correlations (see Appendix A) and molecular simulation data (see Appendix B). For the MacCormack and PPM schemes the spatial correlations of density fluctuations and energy fluctuations have significant spurious oscillations near the correlation point (see Figs. 1 and 3). All three schemes do well in reproducing the expected correlations of momentum fluctuations. Figure 4 depicts $\langle \delta\rho_j\delta J_{j^*} \rangle$, which has a theoretical value of zero since the net flow is zero; all three schemes correctly reproduce this result.

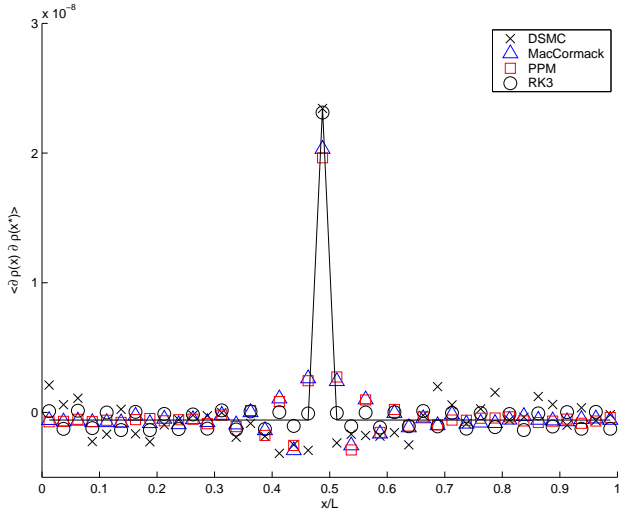


Figure 1: Spatial correlation of density fluctuations. Solid line is $\langle \delta\rho_i\delta\rho_j \rangle = \langle \delta\rho^2 \rangle \delta_{i,j}^K$ (see equations (38, 39)).

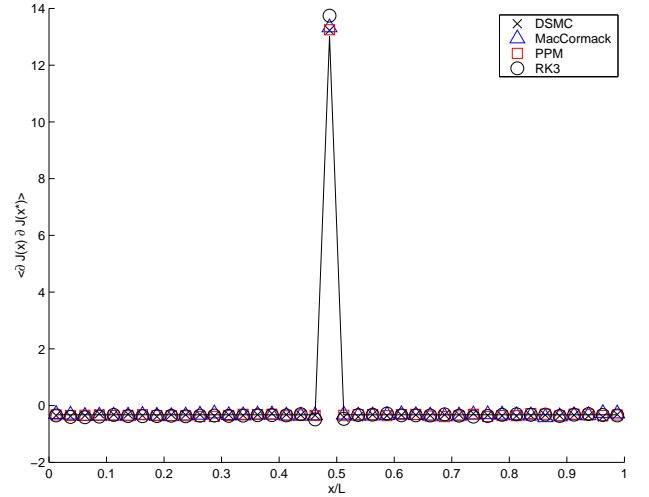


Figure 2: Spatial correlation of momentum fluctuations. Solid line is $\langle \delta J_i\delta J_j \rangle = \langle \delta J^2 \rangle \delta_{i,j}^K$ (see equations (44, 47)).

3.3 Time correlations at equilibrium

The time correlation of density fluctuations is of interest because its temporal Fourier transform gives the spectral density, which is measured experimentally from light scattering spectra [42, 43]. From the LLNS equations, this time correlation can be written as

$$\frac{\langle \delta\rho(w, t)\delta\rho(w, t + \tau) \rangle}{\langle \delta\rho^2(w, t) \rangle} = \left(1 - \frac{1}{\gamma}\right) \exp\{-w^2 D_T \tau\} + \frac{1}{\gamma} \exp\{-w^2 \Gamma \tau\} \cos(c_s w \tau) + \frac{3\Gamma - D_v}{\gamma^2 c_s} w \exp\{-w^2 \Gamma \tau\} \sin(c_s w \tau) \quad (29)$$

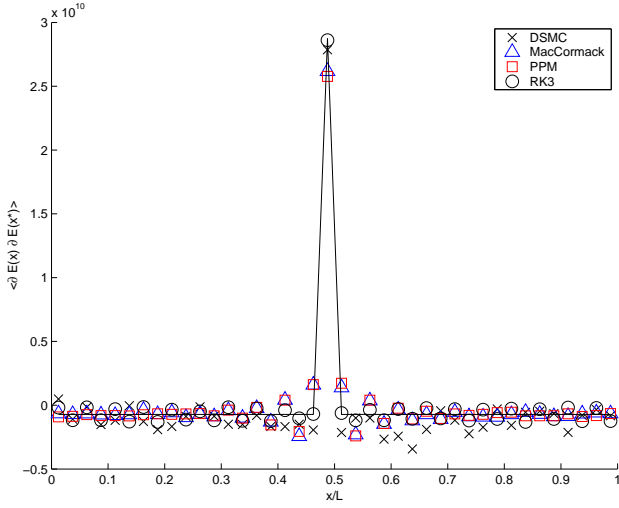


Figure 3: Spatial correlation of energy fluctuations. Solid line is $\langle \delta E_i \delta E_j \rangle = \langle \delta E^2 \rangle \delta_{i,j}^K$ (see equations (46, 48)).

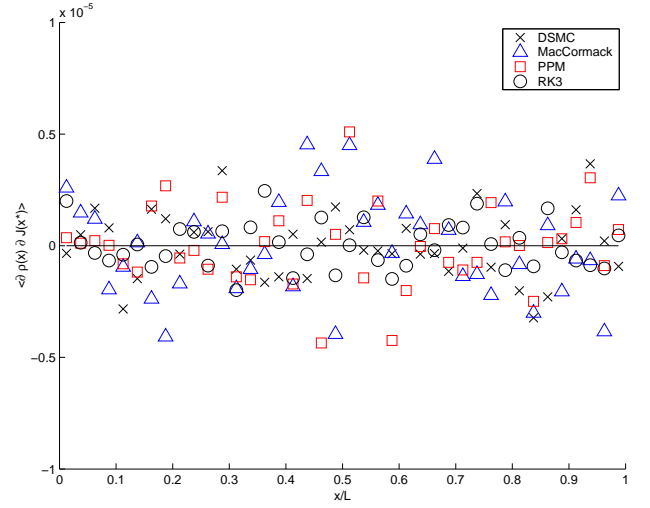


Figure 4: Spatial correlation of density-momentum fluctuations.

where $w = 2\pi n/L$ is the wavenumber, $\gamma = c_p/c_v$ is the ratio of specific heats, $D_T = \kappa/\bar{\rho}c_v$ is the thermal diffusivity, $D_v = \frac{4}{3}\eta/\bar{\rho}$ is the longitudinal kinematic viscosity, c_s is the sound speed, and $\Gamma = \frac{1}{2}[D_v + (\gamma - 1)D_T]$ is the sound attenuation coefficient.

In our numerical calculations the density is represented by cell averages $\rho_i, i = 1, \dots, M_c$, and the time correlation is estimated from the mean of N samples,

$$\langle \delta \rho(w, t) \delta \rho(w, t + \tau) \rangle_N = \frac{1}{N} \sum_{\text{samples}} R(t) R(t + \tau) \quad (30)$$

with

$$R(t) = \frac{1}{M_c} \sum_{i=1}^{M_c} \rho_i \sin(2\pi n x_i / L). \quad (31)$$

We have

$$\langle \delta \rho(w, t) \delta \rho(w, t + \tau) \rangle = \lim_{N \rightarrow \infty} \langle \delta \rho(w, t) \delta \rho(w, t + \tau) \rangle_N. \quad (32)$$

From the above we find the normalization of the theoretical result may be expressed as

$$\begin{aligned} \langle \delta \rho^2(w, t) \rangle = \langle R(t)^2 \rangle &= \frac{1}{M_c^2} \sum_{i=1}^{M_c} \sum_{j=1}^{M_c} \langle \delta \rho_i \delta \rho_j \rangle \sin(2\pi n x_i / L) \sin(2\pi n x_j / L) \\ &= \frac{\langle \delta \rho^2 \rangle}{2M_c}. \end{aligned} \quad (33)$$

We restrict our attention to the lowest wavenumber (i.e., $n = 1$) because for the system sizes we consider the theoretical result, (29), is not accurate at short wavelengths due to mean-free-path corrections.

In the left-hand panel of figure 5, we present time correlation results from our equilibrium problem on a periodic domain. We compare results from the MacCormack, PPM, and RK3 methods with the theoretical time correlation, equation (29), and with molecular simulation data (see Appendix A). We find reasonable agreement among all the results, up to the time when a sound wave has crossed the system ($\approx 4 \times 10^{-9}$ seconds). Due to finite size effects the theory is only accurate for short times but the agreement among the numerical PDE schemes and DSMC molecular simulation is good.

The right-hand panel of figure 5 shows time correlation results for the equilibrium problem on a domain with thermal walls rather than periodic boundaries; we find good agreement for this problem as well, at least for times less than the sound crossing time. For later times, the time correlation is sensitive to the acoustic impedance of the thermal wall. For this case, MacCormack under-predicts the correlation at early time while PPM shows significant deviation near $t = 5 \times 10^{-8}$. Both MacCormack and the RK3 scheme deviate somewhat from DSMC at late time. Overall, however, the RK3 scheme captures the temporal correlation better than either of the other two PDE schemes.

4 Numerical Tests – Non-equilibrium

The results from the section above indicate that of the three stochastic PDE schemes, the third-order Runge-Kutta method (RK3) consistently out-performs the other two schemes. In this section we consider two more numerical tests, spatial correlations in a temperature gradient and diffusion of a standing shock wave, but restrict our attention to the RK3 scheme, comparing it with DSMC molecular simulations.

4.1 Spatial correlations in a temperature gradient

In the early 1980's, a variety of statistical mechanics calculations predicted that a fluid under a non-equilibrium constraint, such as a temperature gradient, would exhibit long-range correlations of fluctuations [44]. Furthermore, quantities that are independent at equilibrium, such as density and momentum fluctuations, also have long-ranged correlations. These predictions were qualitatively confirmed by light scattering experiments [45], yet the effects are subtle and difficult to measure accurately in the laboratory. Molecular simulations confirm the predicted correlations of non-equilibrium fluctuations for a fluid subjected to a temperature gradient [46, 23] and to a shear [47].

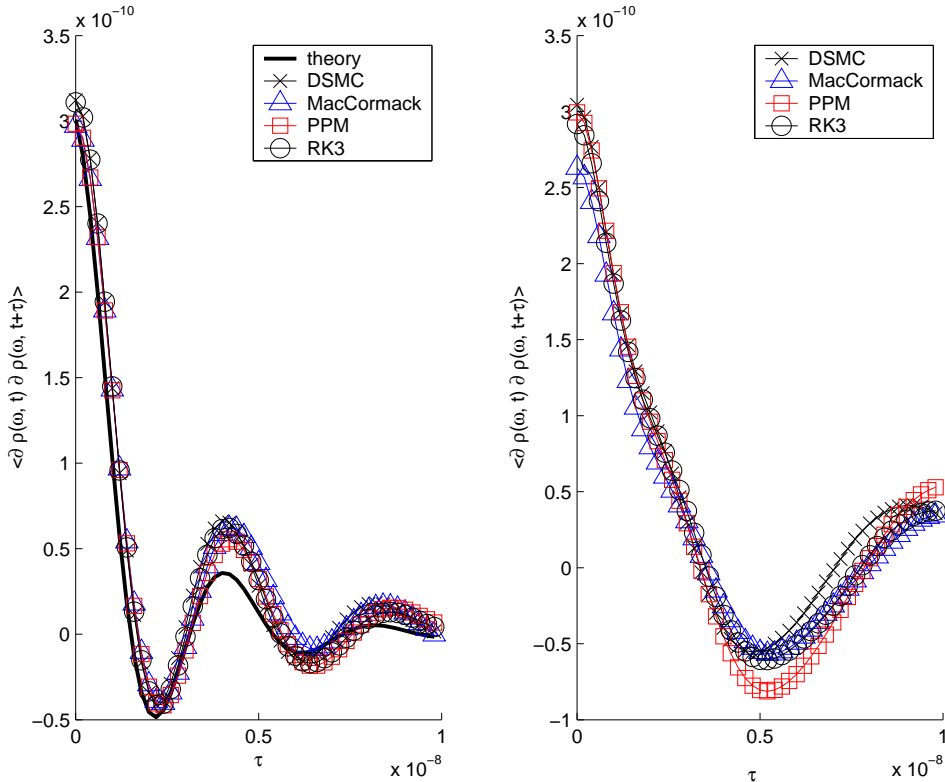


Figure 5: Time correlation of density fluctuations for equilibrium problem, on a periodic domain (left panel) and a domain with specular wall boundaries (right panel).

We consider a system similar to that of section 3.3 but with a temperature gradient. Specifically, the boundary conditions are thermal walls at 273K and 819K. Figure 6 shows the correlation of density and momentum fluctuations measured in an RK3 calculation and by DSMC simulations. The two sets of data are in good agreement and are in agreement with earlier work on this problem [46, 23]. The major discrepancy is the under-prediction of the negative peak correlation near j^* . Extensive tests suggest that this effect is hard to capture with a continuum solver because of the tension between variance reduction and spatial correlations in computing the mass flux at cell edges from cell-centered data.

4.2 Random Walk of a Standing Shock

In our final numerical study we consider the random walk of a standing shock wave due to spontaneous fluctuations. Shock diffusion is well-known in other particle simulations, such as shock tube modeling by DSMC, which must correct for the drift when measuring profiles for steady shocks. [48] The general problem has been also been analyzed for simple lattice gas models [49, 50, 51, 52, 37].

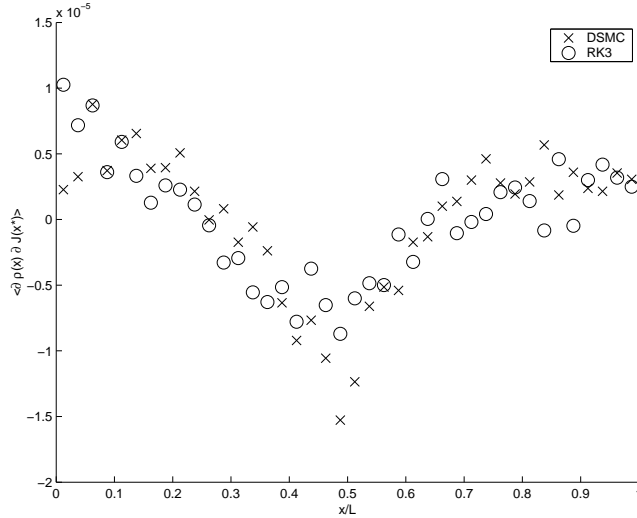


Figure 6: Spatial correlation of density and momentum fluctuations for a system subjected to a temperature gradient. Compare with Fig. 4.

System length	5×10^{-4}	Reference mean free path	6.26×10^{-6}
System volume	7.84×10^{-16}	Time step	1.0×10^{-12}
Number of cells	160	Mach number	2.0
RHS mass density	1.78×10^{-3}	LHS mass density	4.07×10^{-3}
RHS velocity	-61562	LHS velocity	-26933
RHS temperature	273	LHS temperature	567
RHS sound speed	30781	LHS sound speed	44373

Table 3: System parameters (in cgs units) for simulations of a standing shock, Mach 2.0

Mass density and temperature on the right-hand side of the shock are given the same values as in our equilibrium problem; values of density and temperature on the left-hand side are derived from the Rankine-Hugoniot relations. The velocity on both sides of the shock are specified to satisfy the Rankine-Hugoniot conditions and to make the unperturbed shock wave stationary in the computational domain. We consider three different shock strengths, Mach 2, Mach 1.4, and Mach 1.2 (see table 3). The boundary treatment consists of infinite reservoirs with the same states as the initial conditions. For this test problem we use a longer computational domain, in order to capture (unlikely) shock drift of several standard deviations.

Here we focus on the variance of the shock location as a function of time. We define a shock location for density, $\sigma_\rho(t)$ by fitting a Heaviside function to the integrated density,

i.e.,

$$\int_{-L/2}^{\sigma(t)} \rho_L dx + \int_{\sigma_\rho(t)}^{L/2} \rho_R dx = \int_{-L/2}^{L/2} \rho(x, t) dx \quad . \quad (34)$$

Solving for $\sigma_\rho(t)$ gives

$$\sigma_\rho(t) = L \frac{\bar{\rho}(t) - \frac{1}{2}(\rho_L + \rho_R)}{\rho_L - \rho_R} \quad (35)$$

where $\bar{\rho} = L^{-1} \int_{-L/2}^{L/2} \rho(x, t) dx$ is the instantaneous average density. The shock location for pressure, σ_P , is analogously defined. We estimate $\sigma_\rho(t)$ and $\sigma_P(t)$ as functions of time from ensembles of 4000 simulations. For the PDE simulations, we initialize with discontinuous shock profiles. One would expect the shock location to fluctuate with a diffusion similar to that of a simple random walk [51], so averaging over ensembles from the same initial state we would expect to find

$$\langle \delta \sigma_\rho^2 \rangle \approx 2 \mathcal{D}_\rho t \quad \text{and} \quad \langle \delta \sigma_P^2 \rangle \approx 2 \mathcal{D}_P t \quad (36)$$

with shock diffusion coefficients, \mathcal{D}_ρ and \mathcal{D}_P , that depend on shock strength. Note that this expression for the variance is not accurate at very short times (due to transient relaxation from the initial state) or at very long times (due to finite system size).

Figure 7 shows results for the variance in the shock position from an ensemble of runs versus time. After the initial transients, the slopes are constant with the strongest shocks exhibiting the least drift ($\mathcal{D} \cong (\text{Ma} - 1)^{-1}$) and with σ_ρ and σ_P giving similar diffusion coefficients. DSMC data is initially noisy so it has different initial transients and “diffuses” farther than the PDE. However, after the transients, the DSMC and the RK3 simulations have essentially the same slope, as a function of Mach number. This indicates that the third-order Runge-Kutta scheme is accurately capturing the shock-drift random walk.

5 Summary and Concluding Remarks

In this paper we develop and analyze several finite-volume schemes for solving the fluctuating Landau-Lifshitz compressible Navier-Stokes equations in one spatial dimension. Methods based on standard CFD discretizations were found not to accurately represent fluctuations in an equilibrium flow. We have introduced a centered scheme based on interpolation schemes designed to preserve fluctuations combined with a third-order Runge-Kutta (RK3) temporal integrator that was able to capture the equilibrium fluctuations. Further tests for non-equilibrium systems confirm that the RK3 scheme correctly reproduces long-ranged correlations of fluctuations and stochastic drift of shock waves, as verified by comparison with

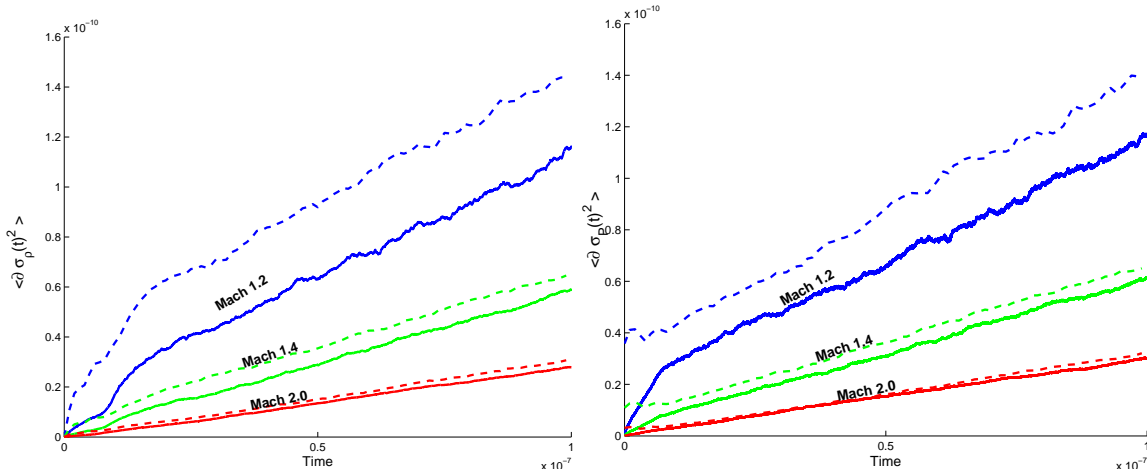


Figure 7: Variance of shock location for mass density profile (left panel, $\langle \delta \sigma_\rho(t)^2 \rangle$) and pressure profile (right panel, $\langle \delta \sigma_P(t)^2 \rangle$). Estimated variances (4000-run ensembles) versus time t for a deterministically steady shock of Mach number 1.2, 1.4, or 2.0. Solid lines are for RK3, dashed lines are from DSMC molecular simulations.

molecular simulations. It is worth emphasizing that the ability of continuum methods to accurately capture fluctuations is fairly sensitive to the construction of the numerical scheme. Minor variations in the numerics can lead to significant changes in stability, accuracy, and behavior.

The work discussed here suggests a number of additional studies. Further analysis is needed on the treatment of thermal and reservoir boundary conditions. The methods here can also be extended to three dimensions (for which the stochastic stress tensor is more complex) and we can include concentration as a hydrodynamic variable to allow the methodology to be applied to a number of other flow problems. Finally, we are integrating our new stochastic PDE solver into our existing Adaptive Mesh and Algorithm Refinement (AMAR) programs [53]. A stochastic AMAR simulation will not only model hydrodynamic fluctuations at multiple grid scales but will, by incorporating DSMC simulations at the finest level of algorithm refinement, also capture molecular-level physics.

Acknowledgment

The authors wish to thank Phil Colella for helpful discussions about the PPM. The work of John Bell was supported by the Applied Mathematics Program of the DOE Office of Mathematics, Information, and Computational Sciences under the U.S. Department of Energy under contract No. DE-AC03-76SF00098. Sarah Williams' support was provided by DE-FC02-01ER25473 SciDAC and DE-FG02-03ER25579 MICS grants.

Appendix A: Equilibrium Fluctuations

For infinite systems, at thermodynamic equilibrium both conserved and hydrodynamic variables are spatially uncorrelated at equal times. For example,

$$\langle \delta\rho_i(t)\delta\rho_j(t) \rangle = \langle \delta\rho^2 \rangle \delta_{i,j}^K. \quad (37)$$

For conserved variables there is a finite size correction, specifically,

$$\langle \delta\rho_i(t)\delta\rho_j(t) \rangle = (1 - M_c^{-1})\langle \delta\rho^2 \rangle \delta_{i,j}^K - M_c^{-1}\langle \delta\rho^2 \rangle (1 - \delta_{i,j}^K) \quad (38)$$

for $i, j = 1, \dots, M_c$, where M_c is the number of cells in the system. The variances are well-known from equilibrium statistical mechanics (§112, [54]).

The variance of mass density depends on the compressibility (i.e., the equation of state) of the fluid. In general,

$$\langle \delta\rho^2 \rangle = \bar{\rho}^2 \frac{\langle \delta N_c^2 \rangle}{\bar{N}_c^2} \quad (39)$$

where \bar{N}_c and $\langle \delta N_c^2 \rangle$ are the mean and variance of the number of particles in a cell. We calculate $\bar{N}_c = \bar{\rho}V_c/m$, where V_c is the volume of a cell and m is the mass of a particle. For an ideal gas N_c is Poisson distributed so $\langle \delta N_c^2 \rangle = \bar{N}_c$ and $\langle \delta\rho^2 \rangle = \bar{\rho}^2/\bar{N}_c$. The more general result is $\langle \delta N_c^2 \rangle = \alpha_T \rho k_B \bar{T} \bar{N}_c/m$ where α_T is the isothermal compressibility.

The variances of fluid velocity and temperature in a cell are

$$\langle \delta u^2 \rangle = \frac{k_B \bar{T}}{\bar{\rho} V_c} = \frac{C_T^2}{\bar{N}_c} \text{ and} \quad (40)$$

$$\langle \delta T^2 \rangle = \frac{k_B \bar{T}^2}{c_v \bar{\rho} V_c} = \frac{C_T^2 \bar{T}}{c_v \bar{N}_c}, \quad (41)$$

where $C_T = \sqrt{k_B \bar{T}/m}$ is the thermal speed (and the standard deviation of the Maxwell-Boltzmann distribution). The covariances are $\langle \delta\rho \delta u \rangle = \langle \delta\rho \delta T \rangle = \langle \delta u \delta T \rangle = 0$.

The variances and covariances of the mechanical densities at equilibrium are

$$\langle \delta\rho \delta J \rangle = \bar{\rho} \bar{J} \Delta_\rho \quad (42)$$

$$\langle \delta\rho \delta E \rangle = \bar{\rho} \bar{E} \Delta_\rho \quad (43)$$

$$\langle \delta J^2 \rangle = \bar{J}^2 \Delta_\rho + \bar{\rho}^2 C_T^2 \Delta_u \quad (44)$$

$$\langle \delta J \delta E \rangle = \bar{J} \bar{E} \Delta_\rho + \bar{J} \rho C_T^2 \Delta_u \quad (45)$$

$$\langle \delta E^2 \rangle = \bar{E}^2 \Delta_\rho + \bar{J}^2 C_T^2 \Delta_u + c_v^2 \bar{\rho}^2 \bar{T}^2 \Delta_T \quad (46)$$

where $\Delta_\rho = \langle \delta\rho^2 \rangle / \bar{\rho}^2$, $\Delta_u = \langle \delta u^2 \rangle / C_T^2$, and $\Delta_T = \langle \delta T^2 \rangle / \bar{T}^2$. For a dilute gas $\Delta_\rho = \Delta_u = 1/\bar{N}_c$, and $\Delta_T = 2/(3\bar{N}_c)$. Again, corrections must be made for conserved quantities in the case of a finite domain:

$$\langle \delta J_i(t) \delta J_j(t) \rangle = (1 - M_c^{-1}) \langle \delta J^2 \rangle \delta_{i,j}^K - M_c^{-1} \langle \delta J^2 \rangle (1 - \delta_{i,j}^K), \quad (47)$$

$$\langle \delta E_i(t) \delta E_j(t) \rangle = (1 - M_c^{-1}) \langle \delta E^2 \rangle \delta_{i,j}^K - M_c^{-1} \langle \delta E^2 \rangle (1 - \delta_{i,j}^K). \quad (48)$$

Appendix B: DSMC Simulations

The algorithms presented here for the stochastic LLNS equations were validated by comparison with molecular simulations. Specifically, we used the direct simulation Monte Carlo (DSMC) algorithm, a well-known method for computing gas dynamics at the molecular scale; see [55, 56] for pedagogical expositions on DSMC, [48] for a complete reference, and [57] for a proof of the method’s equivalence to the Boltzmann equation. As in molecular dynamics, the state of the system in DSMC is given by the positions and velocities of particles. In each time step, the particles are first moved as if they did not interact with each other. After moving the particles and imposing any boundary conditions, collisions are evaluated by a stochastic process, conserving momentum and energy and selecting the post-collision angles from their kinetic theory distributions. DSMC is a stochastic algorithm but the statistical variation of the physical quantities has nothing to do with the “Monte Carlo” portion of the method. The equilibrium and non-equilibrium variations in DSMC are the physical spectra of spontaneous thermal fluctuations, as confirmed by excellent agreement with fluctuating hydrodynamic theory [34, 23] and molecular dynamics simulations [58, 24].

The simulated physical system is a dilute monatomic hard-sphere gas in a rectangular volume with periodic boundary conditions in the y and z directions. The boundary conditions in the x direction are either periodic, specular (i.e., elastic reflection of particles), or a pair of parallel thermal walls. The physical parameters used are presented in Table 1. Samples are taken in forty rectangular cells perpendicular to the x -direction.

References

- [1] R.K. Pathria. *Statistical Mechanics*. Butterworth-Heinemann, Oxford, 1996.
- [2] G. Karniadakis, A. Beskok, and N. Aluru. *Microflows and Nanoflows : Fundamentals and Simulation*. Springer, New York, 2005.
- [3] C.M. Ho ; Y.C. Tai. Micro-electro-mechanical systems (MEMS) and fluid flows. *Annu. Rev. Fluid Mech.*, 30:579–612, 1998.
- [4] M. Gad el Hak. The fluid mechanics of microdevices -the Freeman Scholar lecture. *J. Fluids Eng.*, 121:5–33, 1999.
- [5] B. Alberts, A. Johnson, J. Lewis, M. Raff, K. Roberts, and P. Walter. *Molecular Biology of the Cell*. Garland, New York, 4th edition, 2002.

- [6] R. D. Astumian ; P. Hanggi. Brownian motors. *Physics Today*, pages 33–39, November 2002.
- [7] G. Oster. Darwin’s motors. *Nature*, 417:25, 2002.
- [8] R.K. Soong; G.D. Bachand; H.P. Neves; A.G. Olkhovets; H.G. Craighead; C.D. Montemagno. Powering an inorganic nanodevice with a biomolecular motor. *Science*, 290:1555, 2000.
- [9] T.Y. Tsong. Na,K-ATPase as a Brownian motor: Electric field-induced conformational fluctuation leads to uphill pumping of cation in the absence of ATP. *J. Bio. Phys.*, 28:309–325, 2002.
- [10] H.G. Craighead. Nanoelectromechanical systems. *Science*, 290:1532, 2000.
- [11] A. van Oudenaarden and S.G. Boxer. Brownian ratchets: Molecular separations in lipid bilayers supported on patterned arrays. *Science*, 285:1046–48, 1999.
- [12] J. Bader, R. Hammond, S. Henck, M. Deem, G. McDermott, J. Bustillo, J. Simpson, G. Mulhern, and J. Rothberg. DNA transport by a micromachined Brownian ratchet device. *Proc. Natl. Acad. Sci.*, 96:13165–9, 1999.
- [13] C. Van den Broeck, R. Kawai, and P. Meurs. Exorcising a Maxwell demon. *Phys. Rev. Lett.*, 93:090601, 2004.
- [14] P. Meurs, C. Van den Broeck, and A.L. Garcia. Rectification of thermal fluctuations in ideal gases. *Phys. Rev. E*, 70:051109, 2004.
- [15] B. Nowakowski and A. Lemarchand. Sensitivity of explosion to departure from partial equilibrium. *Physical Review E*, 68:031105, 2003.
- [16] A. Lemarchand and B. Nowakowski. Fluctuation-induced and nonequilibrium-induced bifurcations in a thermochemical system. *Molecular Simulation*, 30(11-12):773–780, 2004.
- [17] L.D. Landau and E.M. Lifshitz. *Fluid Mechanics*, volume 6 of *Course of Theoretical Physics*. Pergamon, 1959.
- [18] M. Bixon and R. Zwanzig. Boltzmann-Langevin equation and hydrodynamic fluctuations. *Phys. Rev.*, 187(1):267–272, Nov 1969.
- [19] R. F. Fox and G. E. Uhlenbeck. Contributions to non-equilibrium thermodynamics. I. Theory of hydrodynamical fluctuations. *Phys. Fluids*, 13(8):1893–1902, 1970.

- [20] G.E. Kelly and M.B. Lewis. Hydrodynamic fluctuations. *Physics of Fluids*, 14(9):1925–1931, 1971.
- [21] E. Calzetta. Relativistic fluctuating hydrodynamics. *Class. Quantum Grav.*, 15:653, 1998.
- [22] P. Espa nol. Stochastic differential equations for non-linear hydrodynamics. *Physica A*, 248:77, 1998.
- [23] M. Malek-Mansour, A.L. Garcia, G.C. Lie, and E. Clementi. Fluctuating hydrodynamics in a dilute gas. *Phys. Rev. Lett.*, 58:874–877, 1987.
- [24] M. Mareschal, M. Malek-Mansour, G. Sonnino, and E. Kestemont. Dynamic structure factor in a nonequilibrium fluid: A molecular-dynamics approach. *Phys. Rev. A*, 45:7180–7183, May 1992.
- [25] A.J.C. Ladd. Short-time motion of colloidal particles: Numerical simulation via a fluctuating lattice-Boltzmann equation. *Phys. Rev. Lett.*, 70(9):1339–1342, Mar 1993.
- [26] N. Sharma and N.A. Patankar. Direct numerical simulation of the Brownian motion of particles by using fluctuating hydrodynamic equations. *J. Comput. Phys.*, 201(2):466–486, 2004.
- [27] M. Moseler and U. Landman. Formation, stability, and breakup of nanojets. *Science*, 289(5482):1165–1169, 2000.
- [28] H.P. Breuer and F. Petruccione. A master equation description of fluctuating hydrodynamics. *Physica A*, 192:569–588, February 1993.
- [29] H.P. Breuer and F. Petruccione. A master equation approach to fluctuating hydrodynamics: Heat conduction. *Phys. Lett. A*, 185:385–389, February 1994.
- [30] M. Serrano and P. Espa nol. Thermodynamically consistent mesoscopic fluid particle model. *Phys. Rev. E*, 64(4):046115, Sep 2001.
- [31] M. Grmela and H.C. Öttinger. Dynamics and thermodynamics of complex fluids. I. Development of a general formalism. *Phys. Rev. E*, 56(6):6620–6632, Dec 1997.
- [32] G. De Fabritiis, P.V. Coveney, and E.G. Flekkøy. Multiscale dissipative particle dynamics. *Philos. Trans. R. Soc. London, Ser. A*, 360:317–331, 2002.
- [33] M. Serrano, G. De Fabritiis, P. Espa nol, E.G. Flekkøy, and P.V. Coveney. Mesoscopic dynamics of Voronoi fluid particles. *J. Phys. A*, 35(7):1605–1625, 2002.

- [34] A.L. Garcia, M. Malek-Mansour, G. Lie, and E. Clementi. Numerical integration of the fluctuating hydrodynamic equations. *J. Stat. Phys.*, 47:209, 1987.
- [35] F.J. Alexander, A.L. Garcia, and D.M. Tartakovsky. Algorithm refinement for stochastic partial differential equations: I. Linear diffusion. *J. Comput. Phys.*, 182(1):47–66, 2002.
- [36] F.J. Alexander, A.L. Garcia, and D.M. Tartakovsky. Algorithm refinement for stochastic partial differential equations: II. Correlated systems. *J. of Comp. Phys.*, 207:769–787, 2005.
- [37] J.B. Bell, J. Foo, and A. Garcia. Algorithm refinement for the stochastic Burgers’ equation. *J. Comp. Phys.*, (in press), 2006.
- [38] P. Colella. A direct Eulerian MUSCL scheme for gas dynamics. *SIAM J. Sci. Stat. Comput*, 6:104–117, 1985.
- [39] P. Colella and P.R. Woodward. The Piecewise Parabolic Method (PPM) for gas-dynamical simulations. *J. of Comp. Phys.*, 54:174–201, 1984.
- [40] R.E. Miller and E.B. Tadmor. The quasicontinuum method: overview, applications and current directions. *J of Comput. Aided Mater. Des.*, 9(3):203–39, 2002.
- [41] P. Colella and H.M. Glaz. Efficient solution algorithms for the Riemann problem for real gases. *J. of Comp. Phys.*, 59:264–289, 1985.
- [42] B. J. Berne and R. Pecora. *Dynamic Light Scattering: With Applications to Chemistry, Biology, and Physics*. Dover, 2000.
- [43] J.P. Boon and S. Yip. *Molecular Hydrodynamics*. Dover, 1991.
- [44] R. Schmitz. Fluctuations in nonequilibrium fluids. *Physics Reports*, 171:1, 1988.
- [45] D. Beysens, Y. Garrabos, and G. Zalczer. Experimental evidence for Brillouin asymmetry induced by a temperature gradient. *Phys. Rev. Lett.*, 45:403, 1980.
- [46] A.L. Garcia. Nonequilibrium fluctuations studied by a rarefied gas simulation. *Phys. Rev. A*, 34:1454, 1986.
- [47] A.L. Garcia, M. Malek-Mansour, G.C. Lie, M. Mareschal, and E. Clementi. Hydrodynamic fluctuations in a dilute gas under shear. *Phys. Rev. A*, 36:4348–4355, 1987.
- [48] G.A. Bird. *Molecular Gas Dynamics and the Direct Simulation of Gas Flows*. Clarendon, Oxford, 1994.

- [49] F.J. Alexander, Z. Cheng, S.A. Janowsky, and J.L. Lebowitz. Shock fluctuations in the two-dimensional asymmetric simple exclusion process. *J. Stat. Phys.*, 68(5-6):761–785, 1992.
- [50] F.J. Alexander, S.A. Janowsky, J.L. Lebowitz, and H. van Beijeren. Shock fluctuations in one-dimensional lattice fluids. *Phys. Rev. E*, 47:403–410, 1993.
- [51] P.A. Ferrari and L.R.G. Fontes. Shock fluctuations in the asymmetric simple exclusion process. *Probab. Theory Related Fields*, 99(2):205–319, 1994.
- [52] S.A. Janowsky and J.L. Lebowitz. Finite-size effects and shock fluctuations in the asymmetric simple-exclusion process. *Phys. Rev. A*, 45:618–625, January 1992.
- [53] A.L. Garcia, J.B. Bell, W.Y. Crutchfield, and B.J. Alder. Adaptive mesh and algorithm refinement using Direct Simulation Monte Carlo. *J. Comput. Phys.*, 154(1):134–155, 1999.
- [54] L.D. Landau and E.M. Lifshitz. *Statistical Physics*, volume 5 of *Course of Theoretical Physics*. Pergamon, third ed., part 1 edition, 1980.
- [55] F.J. Alexander and A.L. Garcia. The Direct Simulation Monte Carlo method. *Computers in Physics*, 11(6):588–593, 1997.
- [56] A.L. Garcia. *Numerical Methods for Physics*. Prentice Hall, 2nd edition, 2000.
- [57] W. Wagner. A convergence proof for Bird’s Direct Simulation Monte Carlo method for the Boltzmann equation. *J. Stat. Phys.*, 66:1011, 1992.
- [58] M. Malek-Mansour, A.L. Garcia, J.W. Turner, and M. Mareschal. On the scattering function of simple fluids in finite systems. *J. Stat. Phys.*, 52:295, 1988.